LETTER

Energetic coupling between plastids and mitochondria drives CO_2 assimilation in diatoms

Benjamin Bailleul[1,2,3,4], Nicolas Berne[1], Omer Murik[4], Dimitris Petroutsos[5], Judit Prihoda[4], Atsuko Tanaka[4], Valeria Villanova[6], Richard Bligny[5], Serena Flori[5], Denis Falconet[5], Anja Krieger-Liszkay[7], Stefano Santabarbara[8], Fabrice Rappaport[3], Pierre Joliot[3], Leila Tirichine[4], Paul G. Falkowski[2], Pierre Cardol[1], Chris Bowler[4] & Giovanni Finazzi[5]

Diatoms are one of the most ecologically successful classes of photosynthetic marine eukaryotes in the contemporary oceans. Over the past 30 million years, they have helped to moderate Earth's climate by absorbing carbon dioxide from the atmosphere, sequestering it via the biological carbon pump and ultimately burying organic carbon in the lithosphere[1]. The proportion of planetary primary production by diatoms in the modern oceans is roughly equivalent to that of terrestrial rainforests[2]. In photosynthesis, the efficient conversion of carbon dioxide into organic matter requires a tight control of the ATP/NADPH ratio which, in other photosynthetic organisms, relies principally on a range of plastid-localized ATP generating processes[3–6]. Here we show that diatoms regulate ATP/NADPH through extensive energetic exchanges between plastids and mitochondria. This interaction comprises the re-routing of reducing power generated in the plastid towards mitochondria and the import of mitochondrial ATP into the plastid, and is mandatory for optimized carbon fixation and growth. We propose that the process may have contributed to the ecological success of diatoms in the ocean.

In oxygenic photosynthesis, light drives a linear electron flow from water to NADPH by the two photosystems (PS I and PS II), and the generation of an electrochemical proton gradient (or proton motive force, PMF) across the thylakoid membranes, which fuels ATP synthesis by an ATP synthase. Although the ratio of ATP/NADPH generated by linear electron flow is not entirely resolved[7,8], it is considered to be insufficient to fuel CO_2 import into the plastid and assimilation by the Calvin cycle[8,9]. Therefore, to make up the shortfall, additional ATP must be produced by alternative pathways that do not generate NADPH. In Viridiplantae (including green algae and higher plants) these alternative electron pathways have been found in the chloroplast and mostly comprise cyclic electron flow (CEF) around PS I (ref. 3) and/or the water-to-water cycles[10]; that is, flows of electrons resulting from the oxidation of water at PS II that are re-routed to an oxidase activity. This last group of oxidases include the Mehler reaction at the PS I acceptor side[4,11,12], the activity of the plastoquinone terminal oxidase downstream of PS II (ref. 5) and the oxygenase activity of ribulose 1,5-bisphosphate carboxylase–oxygenase (Rubisco) (photorespiration[6]). Although genes encoding most components for these processes appear to be present in diatoms[13–15], it is currently unknown what mechanisms are used to balance the ATP/NADPH ratio. We therefore investigated this question using the model species *Phaeodactylum tricornutum*.

The PMF generated across thylakoid membranes comprises an electric field ($\Delta\Psi$) and a proton gradient (ΔpH). The $\Delta\Psi$ can be probed

in vivo by measuring the electro-chromic shift (ECS), that is the Stark effect, a modification of the absorption spectrum of specific pigments caused by changes in the transmembrane electric field in the plastid[16]. An ECS signal is present in *P. tricornutum* (Fig. 1a), and an analysis of the ECS signal relaxation after light exposure (Extended Data Fig. 1) reveals that it comprises two components displaying different spectra (Fig. 1a). One follows a linear dependence on the amplitude of $\Delta\Psi$ whereas the other follows a quadratic relationship (Fig. 1b). The existence of a 'quadratic ECS' is predicted by theory[16] but has only been observed so far in mutants of green algae with altered pigment composition[17]. The peculiar existence of two different ECS probes in wild-type *P. tricornutum* cells allows an absolute quantification of the electric field, providing a valuable tool to analyse the PMF in a living cell (see Methods).

We plotted the amplitude of the quadratic versus linear ECS signals during the relaxation of a light-induced PMF and obtained a parabolic function (Fig. 1c, d and Extended Data Fig. 2). However, the ECS signals did not reach the minimum of the parabola in the dark, but rather remained positive. This indicates that a PMF is maintained across the thylakoid membrane of diatoms in the dark ($\Delta\Psi_d$, Fig. 1c). The field $\Delta\Psi_d$ can not only be dissipated by addition of an uncoupler (carbonyl cyanide-4-(trifluoromethoxy)phenylhydrazone (FCCP)), but also by blocking mitochondrial electron transport by anaerobiosis or addition of antimycin A (AA) plus salicylhydroxamic acid (SHAM). The combination of these two inhibitors blocks both the cyanide-sensitive (complex III) and the cyanide-insensitive (alternative oxidase, AOX) respiratory pathways (Fig. 1d). These results suggest that the residual PMF in the dark is generated in plastids by the chloroplast ATPase by hydrolysis of ATP derived from mitochondria (Fig. 1e)[18]. Furthermore, the extent of $\Delta\Psi_d$ observed in *P. tricornutum* is larger than that previously reported in green algae[19], suggesting that the ATP exchange could be more efficient in diatoms.

To evaluate what mechanism regulates ATP/NADPH in the light in *P. tricornutum*, we first used the linear ECS to probe the CEF capacity (see Methods). CEF turned out to represent only a very low fraction of the maximum electron flow capacity (Fig. 2a and Extended Data Fig. 3a, c) and was insensitive to changes in the photosynthetic flux (Fig. 2a). Thus, it appears very unlikely that CEF could regulate ATP/NADPH fluxes. Next we explored the water-to-water cycle using membrane-inlet mass spectrometry on cells incubated with $^{18}O_2$. O_2 consumption increased with light, being ~2.5-fold higher at saturating light intensities than in the dark (Extended Data Fig. 3b, d). We also found that the light-stimulated O_2 consumption was blocked by 3-(3,4-dichlorophenyl)-1,1-dimethyl-urea (DCMU), which inhibits

[1]Génétique et Physiologie des Microalgues, Département des Sciences de la vie and PhytoSYSTEMS, Université de Liège, B-4000 Liège, Belgium. [2]Environmental Biophysics and Molecular Ecology Program, Departments of Marine and Coastal Sciences and of Earth and Planetary Sciences, Rutgers University, New Brunswick, New Jersey 08901, USA. [3]Institut de Biologie Physico-Chimique (IBPC), UMR 7141, Centre National de la Recherche Scientifique (CNRS), Université Pierre et Marie Curie, 13 Rue Pierre et Marie Curie, F-75005 Paris, France. [4]Ecole Normale Supérieure, PSL Research University, Institut de Biologie de l'Ecole Normale Supérieure (IBENS), CNRS UMR 8197, INSERM U1024, 46 rue d'Ulm, F-75005 Paris, France. [5]Laboratoire de Physiologie Cellulaire et Végétale, UMR 5168, Centre National de la Recherche Scientifique (CNRS), Commissariat à l'Energie Atomique et aux Energies Alternatives (CEA), Université Grenoble Alpes, Institut National Recherche Agronomique (INRA), Institut de Recherche en Sciences et Technologies pour le Vivant (iRTSV), CEA Grenoble, F-38054 Grenoble cedex 9, France. [6]Fermentalg SA, F-33500 Libourne, France. [7]Institute for Integrative Biology of the Cell (I2BC), Commissariat à l'Energie Atomique et aux Energies Alternatives (CEA), Centre National de la Recherche Scientifique (CNRS), Université Paris-Sud, Institut de Biologie et de Technologie de Saclay, F-91191 Gif-sur-Yvette cedex, France. [8]Istituto di Biofisica, Consiglio Nazionale delle Ricerche, Via Celoria 26, I-20133 Milan, Italy.

Figure 1 | ECS measures the PMF in *P. tricornutum*. a, Deconvolution of the experimental ECS spectrum (black) into linear (blue) and quadratic (red) spectral components (see Methods); r.u., relative units. **b**, Schematic representation of polar (blue) and polarizable (red) pigments, and their associated linear (blue) and quadratic (red) ECS responses to the electric field. Black: thylakoid lipid bilayer. Green '+' and '−' symbols: $\Delta\Psi$. Red arrows: pigment polarization induced by $\Delta\Psi$. **c, d**, Relationship between quadratic and linear ECS in control (**c**) and in cells treated with uncoupler (8 μM FCCP, black squares), anaerobiosis (red circles) and respiratory inhibitors (AA, 5 μM, and SHAM, 1 mM; blue circles) (**d**). Green arrow: extent of the dark electric field ($\Delta\Psi_d$). Representative of five (**c**) and three (**d**) independent biological samples. **e**, Schematic representation of the energetic interactions between plastid (left) and mitochondria (right) in the dark. Red arrows: respiratory electron flows. Green dashed line: putative ATP/ADP exchange pathway between the organelles. ATPase, ATPase/synthase; b_6f, cytochrome b_6f; I/III/IV, respiratory complexes I, III and IV.
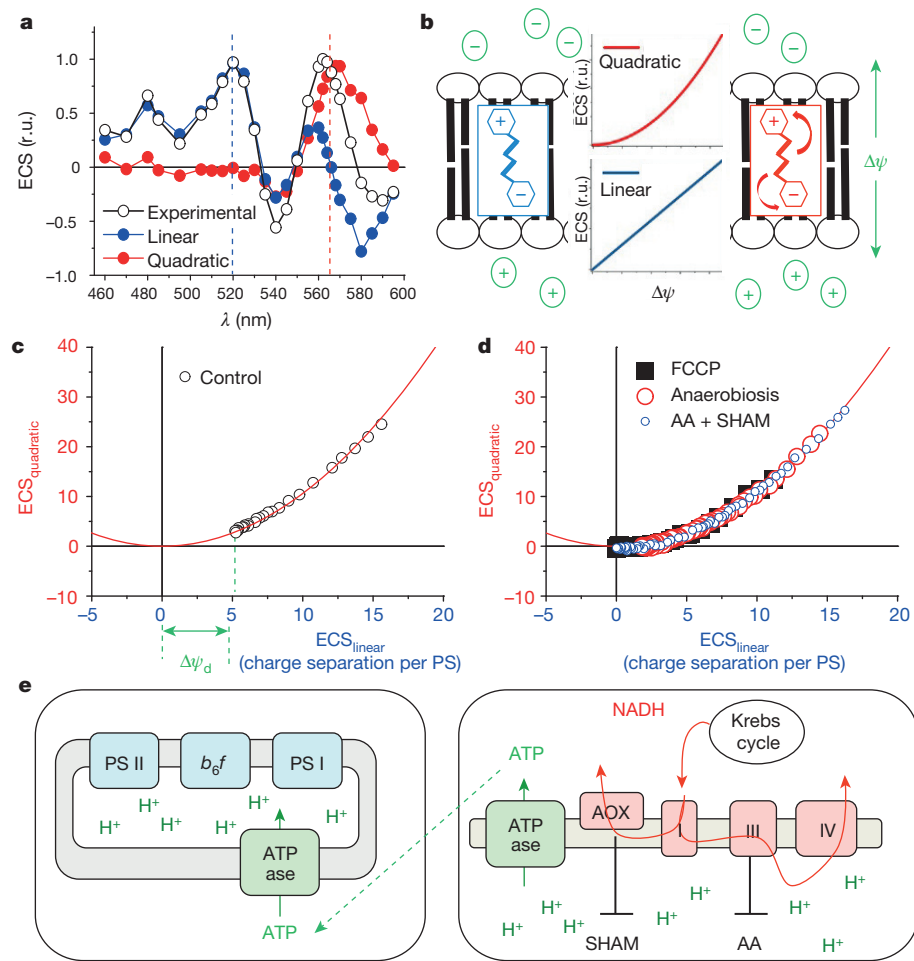
O$_2$ production by PS II (Extended Data Fig. 3b, d), indicating that this process is fed by electrons generated by PS II. O$_2$ consumption increased linearly with O$_2$ production, in agreement with earlier findings in another diatom species[20], indicating that a constant proportion (~10%) of the electron flow from photosynthesis is re-routed to an O$_2$-consuming pathway, regardless of light intensity (Fig. 2b).

To test whether the O$_2$-consuming pathway occurs in the plastid or relies on mitochondrial activity, we used increasing concentrations of inhibitors to titrate respiration and tested possible consequences on photosynthesis. We reasoned that if respiration consumes reducing equivalents generated in the plastid to generate additional ATP, any mitochondrial dysfunction should negatively impact photosynthesis.
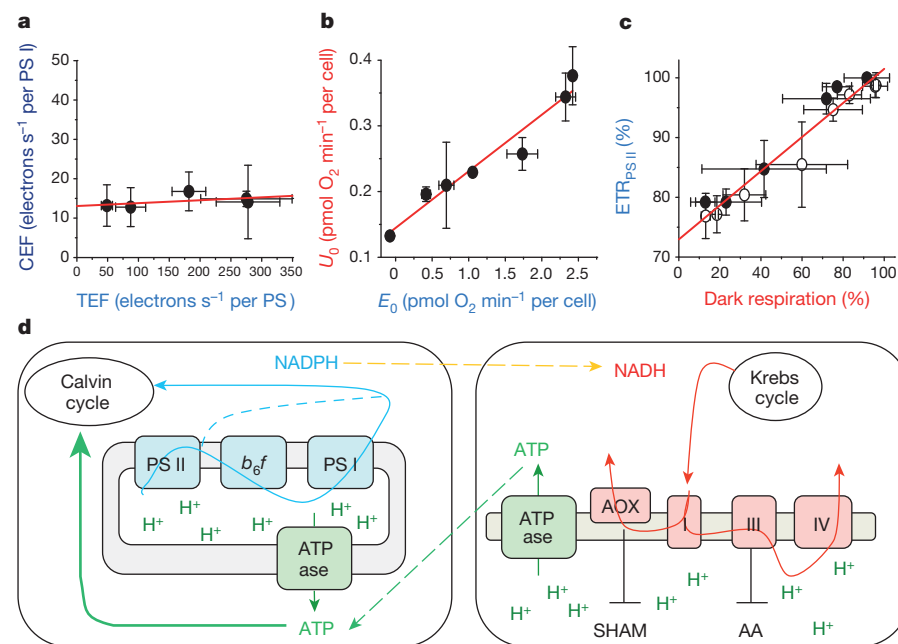
Figure 2 | Energetic interactions between mitochondria and plastid in *P. tricornutum*. a, Relationship between CEF capacity and total electron flow (TEF, mean ± s.d. from data in Extended Data Fig. 3a, c). **b**, Relationship between oxygen uptake (U_0) and gross photosynthesis (E_0) as measured by membrane-inlet mass spectrometry (mean ± s.e.m. from data in Extended Data Fig. 3b, d). **c**, Dependency of photosynthetic activity (ETR$_{PS II}$) on respiration rates (as the percentage of control, mean ± s.d. from data in Extended Data Fig. 4). Closed circles: SHAM + AA; open circles: SHAM + myxothiazol treatments (see Methods). **d**, Schematic representation of possible plastid–mitochondria metabolic interactions in the light. Continuous and dashed blue arrows: photosynthetic linear and cyclic flows, respectively. Yellow arrow: exchange of reducing equivalents. For other symbols, see text and Fig. 1e.
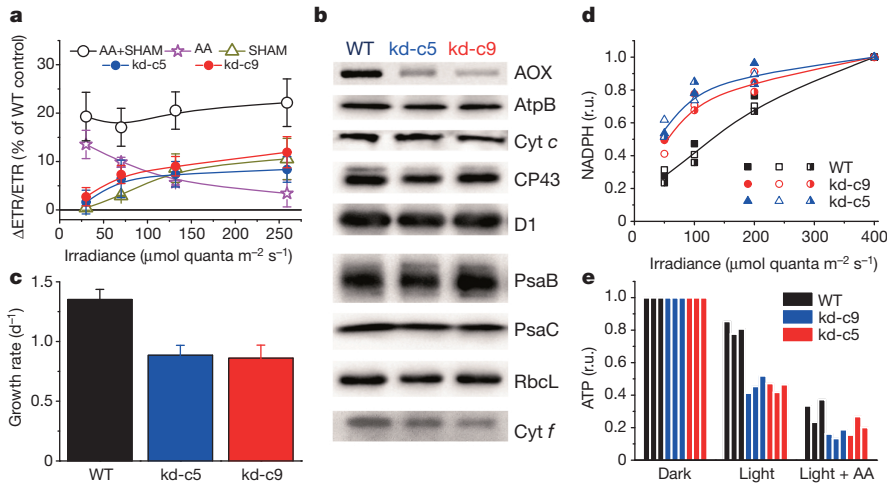
Figure 3 | Phenotypic traits of AOX knockdown lines of *P. tricornutum*. **a**, Relative sensitivity of photosynthesis (ETR$_{PS II}$) to addition of respiratory inhibitors: AA (magenta), SHAM (dark yellow) and AA + SHAM (black) ($n = 3 \pm$ S.D), or to knockdown of AOX ($n = 5 \pm$ s.d.). Blue and red: kd-c5 and kd-c9, respectively. **b**, Western blot analysis of photosynthetic and respiratory complexes. **c**, Growth rates of the wild-type and AOX lines ($n = 7 \pm$ s.d.). **d**, *In vivo* light dependency of NADPH redox state in wild-type and AOX lines. Data are normalized to the maximum value in the light. **e**, *In vivo* ^{31}P-NMR evaluation of the NTP content in wild-type and AOX knockdown lines, in the dark or in low light, with or without AA (data normalized to the dark values). **d**, **e**, Three independent biological samples.

We found that this was indeed the case, as photosynthetic electron transfer rate (ETR$_{PS II}$) linearly followed changes in respiration (Fig. 2c and Extended Data Fig. 4). We conclude that a partial re-routing of the photosynthetic flow towards mitochondrial respiration rather than CEF optimizes photosynthesis in diatoms, providing commensurate ATP per NADPH at all irradiances (Fig. 2d).

Photosynthetic activity displayed increasing sensitivity to AOX inhibition with light, suggesting that cyanide-insensitive respiration becomes prominent in high light (Fig. 3a). This prompted us to generate AOX knockdown cell lines of *P. tricornutum*. Two independent clones were selected on the basis of reduced AOX protein accumulation (Fig. 3b) and decreased activity (measured as the SHAM-sensitive, AA-insensitive component of respiration; Extended Data Fig. 5a). The AOX contribution, representing ~50% of dark respiration in wild-type cells (Extended Data Fig. 4e), was decreased two-fold in the two knockdown lines (Extended Data Fig. 5a). Confocal microscopy confirmed the mitochondrial localization of the targeted gene product (Extended Data Fig. 6a). The reduced AOX activity in the knockdown lines paralleled a diminished PMF in the dark ($\Delta\Psi_d$, Extended Data

Fig. 5b), despite the fact that overall dark respiration was slightly higher (Extended Data Fig. 5a). This effect was strongly enhanced by addition of AA (Extended Data Fig. 5b). The decreased AOX activity also correlated with a decreased photosynthetic capacity, especially under high light intensities (similar to SHAM-treated wild-type cells; Fig. 3a), and a diminished growth rate (Fig. 3c), which was exacerbated further by inhibiting complex III using AA (Extended Data Fig. 5c). The growth and photosynthetic phenotypes were not due to changes in the accumulation of the photosynthetic complexes, for which we detected comparable levels of representative proteins in all cell lines (Fig. 3b). The only exception was a small decrease in the cytochrome b_6f content in the knockdown cell lines, which nonetheless did not decrease its overall catalytic turnover (Extended Data Fig. 7).

Our working model presented in Fig. 2d predicts that disruption of the plastid–mitochondria interaction in the knockdown cell lines should lead to the accumulation of NADPH and a decreased cellular content of ATP in the light. Indeed, *in vivo* assessments of the pools of NADPH and ATP in wild-type and knockdown cell lines confirmed an increase in the NADPH/NADP$^+$ ratio with light intensity
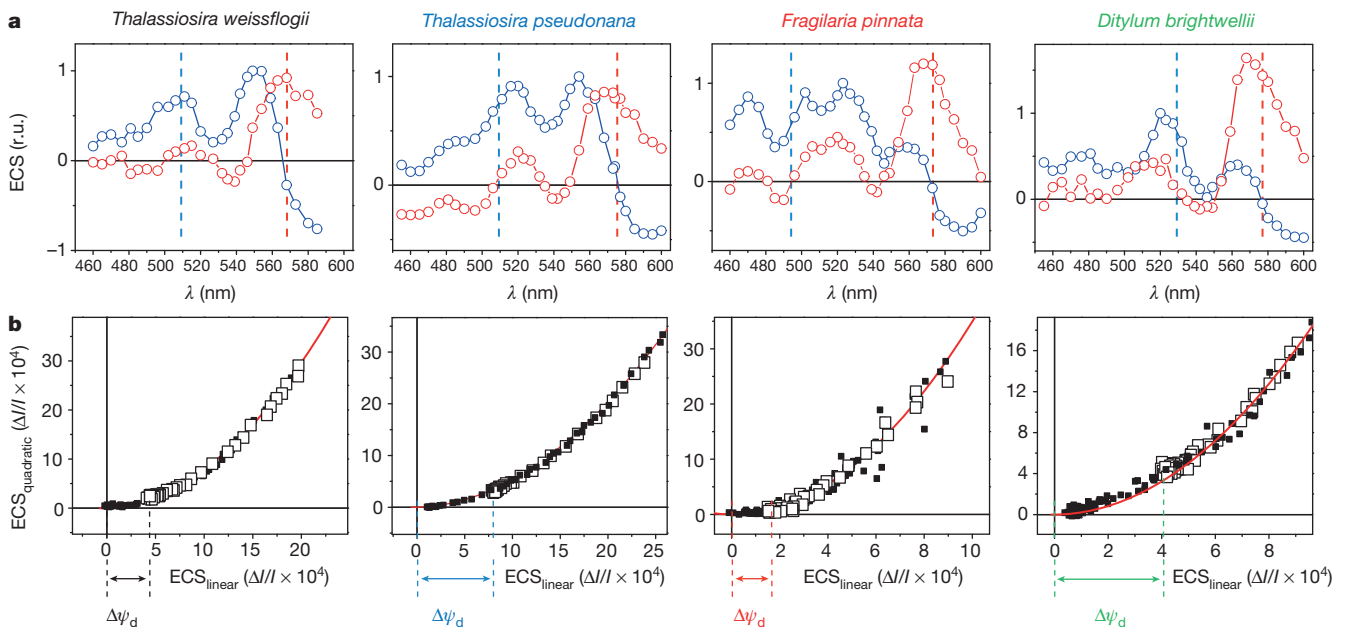
Figure 4 | ATP transfer from mitochondria to plastid in representative diatoms. **a**, Spectra of the linear (blue) and quadratic (red) ECS probes in four diatoms. Blue and red vertical dashed lines represent the wavelengths used for linear and quadratic ECS, respectively. Spectra are normalized to 1 at the maximum value of the linear ECS. **b**, Relationship between the quadratic and the linear ECS in control conditions (open symbols) and in AA + SHAM conditions (filled symbols). $\Delta\Psi_d$ is represented as a horizontal arrow. Data are representative of three independent biological samples.

(Fig. 3d and Extended Data Fig. 8a), accompanied by a net decrease of cellular ATP levels (Fig. 3e and Extended Data Fig. 8b), both of which were more drastic in AOX knockdown cells than wild-type cells. These observations confirm that mitochondrial respiration is directly involved in the adjustment of the ATP to NADPH ratio in the plastid.

We then examined the generality of our findings in other diatom species. The similar ECS features (linear and quadratic components) in *Thalassiosira pseudonana*, *Thalassiosira weissflogii*, *Fragilaria pinnata* and *Ditylum brightwellii* (Fig. 4a) were used to confirm the presence of a PMF in the plastids in the dark at the expense of hydrolysis of ATP supplied by the mitochondria in all cases (Fig. 4b). Moreover, a negligible contribution of CEF (Extended Data Fig. 9) and a significant involvement of mitochondrial respiration to photosynthesis (Extended Data Fig. 10) were found in all these species. The involvement of mitochondrial respiration in the optimization of photosynthesis therefore appears to be a general and conserved feature in diatoms.

We conclude that ATP generation sets the rate of photosynthetic carbon assimilation in diatoms, as suggested in other photosynthetic organisms[8], but that in contrast with the Viridiplantae, optimization of diatom photosynthesis does not rely on plastid-localized processes. Instead, constitutive energetic interactions between diatom mitochondria and plastids ensure the sharing of reducing equivalents and ATP to fuel CO_2 assimilation in the light (Fig. 2d). While the process we have uncovered has some similarities to the export of reducing equivalents from the plastids towards mitochondria in plants and green algae, the fundamental difference is that in plants and green algae the process serves as a valve to dissipate excess of reducing power[21], and can only participate in the regulation of the ATP/NADPH ratio when the chloroplast capacity to make extra ATP is genetically disrupted[22–24]. We propose that the presence of transporters such as the malate shuttle[21], which are encoded in diatom genomes[13], as well as the very tight physical interactions observed in diatoms between plastids and mitochondria (Extended Data Fig. 6b), may make these energetic interactions possible between the two organelles. Because diatom plastids are surrounded by four membranes rather than two as in Viridiplantae[13], it will be of interest to elucidate the configuration of such transporters, as well as the rationale for the diminished CEF efficiency in diatoms. More generally, the coupling of respiratory and photosynthetic activities in diatoms should be explored in the context of resource utilization in the ocean and as a means to boost the production of useful metabolites for biotechnology.

Online Content Methods, along with any additional Extended Data display items and Source Data, are available in the online version of the paper; references unique to these sections appear only in the online paper.

Received 16 January; accepted 28 May 2015.
Published online 13 July; corrected online 19 August 2015 (see full-text HTML version for details).

1. Falkowski, P. G. The evolution of modern eukaryotic phytoplankton. *Science* **305**, 354–360 (2004).
2. Field, C. B., Behrenfeld, M. J., Randerson, J. T. & Falkowski, P. G. Primary production of the biosphere: integrating terrestrial and oceanic components. *Science* **281**, 237–240 (1998).
3. Shikanai, T. Cyclic electron transport around photosystem I: genetic approaches. *Annu. Rev. Plant Biol.* **58**, 199–217 (2007).
4. Asada, K. The water–water cycle as alternative photon and electron sinks. *Phil. Trans. R. Soc. Lond. B* **355**, 1419–1431 (2000).
5. Cardol, P. *et al.* An original adaptation of photosynthesis in the marine green alga *Ostreococcus*. *Proc. Natl Acad. Sci. USA* **105**, 7881–7886 (2008).
6. Ort, D. R. & Baker, N. R. A photoprotective role of O_2 as an alternative electron sink in photosynthesis? *Curr. Opin. Plant Biol.* **5**, 193–198 (2002).
7. Petersen, J., Förster, K., Turina, P. & Gräber, P. Comparison of the H^+/ATP ratios of the H^+-ATP synthases from yeast and from chloroplast. *Proc. Natl Acad. Sci. USA* **109**, 11150–11155 (2012).
8. Allen, J. F. Photosynthesis of ATP-electrons, proton pumps, rotors, and poise. *Cell* **110**, 273–276 (2002).
9. Lucker, B. & Kramer, D. M. Regulation of cyclic electron flow in *Chlamydomonas reinhardtii* under fluctuating carbon availability. *Photosynth. Res.* **117**, 449–459 (2013).
10. Allen, J. F. Oxygen reduction and optimum production of ATP in photosynthesis. *Nature* **256**, 599–600 (1975).
11. Radmer, R. J. & Kok, B. Photoreduction of O_2 primes and replaces CO_2 assimilation. *Plant Physiol.* **58**, 336–340 (1976).
12. Badger, M. R. Photosynthetic oxygen exchange. *Annu. Rev. Plant Physiol.* **36**, 27–53 (1985).
13. Prihoda, J. *et al.* Chloroplast-mitochondria cross-talk in diatoms. *J. Exp. Bot.* **63**, 1543–1557 (2012).
14. Bowler, C. *et al.* The *Phaeodactylum* genome reveals the evolutionary history of diatom genomes. *Nature* **456**, 239–244 (2008).
15. Grouneva, I., Rokka, A. & Aro, E.-M. The thylakoid membrane proteome of two marine diatoms outlines both diatom-specific and species-specific features of the photosynthetic machinery. *J. Proteome Res.* **10**, 5338–5353 (2011).
16. Witt, H. T. Energy conversion in the functional membrane of photosynthesis. Analysis by light pulse and electric pulse methods. The central role of the electric field. *Biochim. Biophys. Acta* **505**, 355–427 (1979).
17. Joliot, P. & Joliot, A. Characterization of linear and quadratic electrochromic probes in *Chlorella sorokiniana* and *Chlamydomonas reinhardtii*. *Biochim. Biophys. Acta* **975**, 355–360 (1989).
18. Diner, B. & Joliot, P. Effect of the transmembrane electric field on the photochemical and quenching properties of photosystem II *in vivo*. *Biochim. Biophys. Acta* **423**, 479–498 (1976).
19. Finazzi, G. & Rappaport, F. *In vivo* characterization of the electrochemical proton gradient generated in darkness in green algae and its kinetics effects on cytochrome b_6f turnover. *Biochemistry* **37**, 9999–10005 (1998).
20. Waring, J., Klenell, M., Bechtold, U., Underwood, G. J. C. & Baker, N. R. Light-induced responses of oxygen photo-reduction, reactive oxygen species production and scavenging in two diatom species. *J. Phycol.* **46**, 1206–1217 (2010).
21. Kinoshita, H. *et al.* The chloroplastic 2-oxoglutarate/malate transporter has dual function as the malate valve and in carbon/nitrogen metabolism. *Plant J.* **65**, 15–26 (2011).
22. Lemaire, C., Wollman, F. A. & Bennoun, P. Restoration of phototrophic growth in a mutant of *Chlamydomonas reinhardtii* in which the chloroplast atpB gene of the ATP synthase has a deletion: an example of mitochondria-dependent photosynthesis. *Proc. Natl Acad. Sci. USA* **85**, 1344–1348 (1988).
23. Cardol, P. *et al.* Impaired respiration discloses the physiological significance of state transitions in *Chlamydomonas*. *Proc. Natl Acad. Sci. USA* **106**, 15979–15984 (2009).
24. Dang, K. V. *et al.* Combined increases in mitochondrial cooperation and oxygen photoreduction compensate for deficiency in cyclic electron flow in *Chlamydomonas reinhardtii*. *Plant Cell* **26**, 3036–3050 (2014).

METHODS

No statistical methods were used to predetermine sample size. The experiments were not randomized. The investigators were not blinded to allocation during experiments and outcome assessment.

Growth conditions. Wild-type and AOX transformant lines of *P. tricornutum* Pt1 8.6 (CCMP 2561) were grown in artificial sea water (ASW[25]). *T. pseudonana* (CCMP 1335), *T. weissflogii* (CCMP 1336), *F. pinnata* (CCAP 1029/2) and *D. brightwellii* (CCMP 359) were grown in F/2 medium, supplemented with silicate[26]. All strains were grown at $19 \pm 1\,^{\circ}\mathrm{C}$ in semi-continuous batch culture (with moderate shaking for *P. tricornutum, T. pseudonana* and *T. weissflogii*). The photoperiod was 12 h light/12 h dark, and light irradiance was $70\,\mu\mathrm{mol}$ quanta $\mathrm{m}^{-2}\,\mathrm{s}^{-1}$. Cell concentration was determined daily with a Z2 Coulter Counter analyser (Beckman Coulter) to ensure all the experiments were performed with cells in exponential phase. For biophysical measurements, cells were concentrated by centrifugation and resuspended in their growth medium (supplemented with 10% w/v Ficoll to prevent cell sedimentation) and kept in the dark at least 30 min before measurements.

Inhibitors. DCMU, 2,5-dibromo-3-methyl-6-isopropyl-p-benzoquinone (DBMIB), FCCP, AA, myxothiazol and SHAM (Sigma-Aldrich) were dissolved in ethanol, whereas hydroxylamine, glucose, glucose oxidase and catalase (Sigma-Aldrich) were dissolved in deionized water. FCCP was used at a very low concentration (8 μM, Fig. 1d) to allow the disruption of the dark PMF without preventing the light-induced generation of PMF needed to quantify $\Delta\Psi_\mathrm{d}$. AA and myxothiazol were used at 5 μM, unless otherwise stated. DCMU was used at a concentration of 15 μM. In every measurement involving hydroxylamine or SHAM, the lowest inhibitor concentration to induce a full inhibition of PS II activity or maximum inhibition of respiration, respectively, was used. The range of concentrations used was 30–100 μM and 0.5–1 mM for hydroxylamine and SHAM, respectively. Anaerobic conditions were obtained through incubation with catalase (1,000 U ml^{-1}), glucose (10 mM) and glucose oxidase (20,000 U ml^{-1}). AA has been previously described as an inhibitor of cyclic electron flow, affecting the NDH-independent pathway[27]. This potential effect was ruled out in diatoms because no change in cyclic electron flow was noticed upon addition of AA. Consistent with the fact that genes encoding some members of the NDH complex are absent in diatom genomes, this indicates that AA does not affect the NDH-independent CEF pathway in diatoms. AA and myxothiazol were preferred to potassium cyanide to block the cyanide sensitive pathway of respiration because potassium cyanide also affects Rubisco activity[28], ascorbate peroxidase[29] and Cu/Zn superoxide dismutase[30].

Deconvolution of linear and quadratic ECS components. To deconvolute the linear and quadratic contributions to the ECS signals, cells were left for an hour in the cuvette to reach complete anaerobiosis. In these conditions, the ATP synthase activity is slowed down[31], and long-living ECS signals are no longer contaminated with other light-induced absorption changes (principally associated with *c*-type cytochromes). Light stimulation of cells was achieved with a series of six laser single-turnover (duration ∼7 ns) saturating flashes, provided by a laser dye (LDS 698) pumped by a frequency doubled Nd-YAG laser (Quantel). We considered that the relaxation of the electric field generated by the light stimulus is described by the exponential function $\Delta\Psi = \Delta\Psi_0 \exp(-t/\tau)$, where t is time, $\Delta\Psi_0$ is the initial electric field generated by the light, and τ is the electric-field decay lifetime. The linear and quadratic components of the ECS are theoretically proportional to $\Delta\Psi$ and $\Delta\Psi^2$, respectively. Therefore, the $\Delta I/I$ spectro-temporal matrices (from 460 to 600 nm) can be described by a sum of two exponentials: $y(\lambda,t) = A(\lambda) \exp(-t/\tau) + B(\lambda) \exp((-2t/\tau)) + C(\lambda)$. The kinetics of ECS relaxation were fitted by a global routine, which considers the lifetime τ as a global (wavelength-independent) variable, and the amplitudes of linear and quadratic components (A and B, respectively) as local (wavelength-dependent) variables. A non-decaying component (C) was also included in the fit to account for a small fraction of residual signal at long delay times. The plot of the A and B amplitudes as a function of the wavelength provides the decay associated spectra of the linear and quadratic contributions to the ECS signal, respectively, which are shown in Fig. 1a. The fit was performed with homemade software, which used the MINUIT package, developed and distributed by CERN (Geneva, Switzerland) and implemented in FORTRAN77. It minimizes the reduced sum of squared residues between the model function and the experimental data, employing a two-step protocol involving an initial search that utilizes the Simplex method (Nelder–Mead algorithm) and a refined search using the Levenberg–Marquardt algorithm as described in ref. 32. The quality of the fit description was judged on the basis of reduced sum of squared residues statistics, visual inspection of the fit residuals, residuals autocorrelation and stability of the solutions upon random perturbation of the best-fit. The deconvolution was performed on two independent biological samples, giving similar results.

Measurements of *c*-type cytochromes and linear and quadratic ECS. Absorption difference signals were measured at different wavelengths with a Joliot-type spectrophotometer (JTS-10, Biologic), equipped with a white probing LED and the appropriate interference filters (3–8 nm bandwidth). For $\Delta\Psi_\mathrm{d}$ measurements, the PMF was increased using an ∼10 ms pulse of saturating (4,500 μmol quanta m^{-2} s^{-1}) red light (see Extended Data Fig. 3 for representative ECS kinetics). For *P. tricornutum*, ECS signals were evaluated using three wavelengths, to eliminate contribution from *c*-type cytochrome*s* (see Extended Data Fig. 2). The latter was calculated as cyt $c = [554] - 0.4[520] - 0.4[566]$, where [554], [520] and [566] are the absorption difference signals at 554 nm, 520 nm and 566 nm, respectively. The very similar relaxation of *c*-type cytochromes in aerobic and anaerobic conditions, despite very different ECS relaxations (Extended Data Fig. 2b), demonstrates the validity of the cyt *c* deconvolution procedure. Then, ecs$_\mathrm{lin}$ and ecs$_\mathrm{quad}$ (ECS signals before correction for $\Delta\Psi_\mathrm{d}$) were estimated from the following relationships: ecs$_\mathrm{lin} = [520] - 0.25$cyt c and ecs$_\mathrm{quad} = [566] + 0.15$cyt c. For the other diatoms, appropriate wavelengths were chosen for calculating ecs$_\mathrm{lin}$ and ecs$_\mathrm{quad}$ (red and blue lines in Fig. 4) to minimize the cytochrome *c* contributions. The relationships between ecs$_\mathrm{quad}$ and ecs$_\mathrm{lin}$ were fitted with the parabolic equation ecs$_\mathrm{quad} + a\Delta\Psi_\mathrm{d}^2 = a(\mathrm{ecs}_\mathrm{lin} + \Delta\Psi_\mathrm{d})^2$, where $\Delta\Psi_\mathrm{d}$ is the electrical component of the PMF in the dark and a is constant for all the conditions in a diatom species (see Extended Data Fig. 2c). The ecs$_\mathrm{lin}$ and ecs$_\mathrm{quad}$ values represent ECS changes relative to dark values. Therefore, we corrected them for the dark electric field. This leads to ECS$_\mathrm{lin} = \mathrm{ecs}_\mathrm{lin} + \Delta\Psi_\mathrm{d}$, and ECS$_\mathrm{quad} = \mathrm{ecs}_\mathrm{quad} + a\Delta\Psi_\mathrm{d}^2$, namely absolute values of the ECS signals. This simply corresponds to a shift of the *x*- and *y*-axes to allow the minimum of the parabola to coincide with the origin of the axes (see Extended Data Fig. 2d), and gives ECS$_\mathrm{quad} = a\mathrm{ECS}_\mathrm{lin}^2$. This leads to the evaluation of $\Delta\Psi_\mathrm{d}$ as the minimal ECS$_\mathrm{lin}$ value of the experimental data. In Fig. 1c, d, and Extended Data Fig. 2c, d, ECS data were normalized to the ecs$_\mathrm{lin}$ increase upon a saturating laser flash (that is, one charge separation per photosystem, see ref. 33). This allows the estimation of $\Delta\Psi_\mathrm{d}$ in *P. tricornutum* as approximately five charge separations by PS, namely ∼100 mV (ref. 12) (Fig. 1c). The presence of linear and quadratic ECS components allows measurement of the absolute value of $\Delta\Psi$ in the dark ($\Delta\Psi_\mathrm{d}$). Indeed the amplitude of the linear ECS response (ecs$_\mathrm{lin}$) observed upon a light stimulus increasing $\Delta\Psi$ is constant, namely independent of the value of the field pre-existing the illumination ($\Delta\Psi_\mathrm{d}$). Conversely, the amplitude of the quadratic ECS response (ecs$_\mathrm{quad}$) is a function of the value of $\Delta\Psi_\mathrm{d}$. Therefore, plotting the amplitude of the ecs$_\mathrm{quad}$ versus ecs$_\mathrm{lin}$ allows quantification of the absolute value of the electric field in the dark ($\Delta\Psi_\mathrm{d}$).

Cyt b_6f turnover was measured through the slow phase (phase b[31]) of the linear ECS, which reflects b_6f-catalysed charge transfer across the membranes, and through the reduction rate of the *c*-type cytochromes (c_6/f), using the three-wavelengths deconvolution procedure described above. Measurements were performed after a saturating laser flash.

Measurements of photosynthetic flows. For calculation of the TEF (the sum of linear and cyclic electron flows) and CEF capacities, we measured the photochemical rates in the absence and presence, respectively, of DCMU. In brief, under steady-state illumination conditions, the ECS signal results from concomitant transmembrane potential generation by PS II, the cytochrome b_6f complex and PS I, and from transmembrane potential dissipation by the plastid ATP synthase. When light is switched off, PS activities stop immediately, while ATP synthase and cytochrome b_6f complex activities remain (transiently) unchanged. Therefore, the difference between the slopes of the linear ECS signal (ECS$_\mathrm{lin}$) measured in the light and after the light is switched off ($S_\mathrm{D} - S_\mathrm{L}$) is proportional to the rate of PS I and PS II photochemistry (that is, to the rate of 'total' electron flow, Extended Data Fig. 3a). Because the linear ECS has been normalized to the amplitude of the linear ECS signal induced by a saturating laser flash[34] (see above), the difference of slopes evaluates the number of charge separations per photosystem and per second. The rate of CEF can be evaluated using the same approach under conditions where PS II activity is inhibited by DCMU, and dividing this slope by the linear ECS signal induced by a saturating laser flash in the presence of PS II inhibitors (one charge separation per PS I (ref. 34)). This was done using saturating concentrations of DCMU, which block PS II oxidation, and of hydroxylamine, to avoid charge recombination within PS II.

Fluorescence-based measurements. Fluorescence-based photosynthetic parameters were measured with a fluorescence imaging setup described in ref. 35. Photosynthetic electron transfer rate ETR$_\mathrm{PS\,II}$ and NPQ were calculated, respectively, as $I(F_\mathrm{m}' - F)/F_\mathrm{m}'$ and $(F_\mathrm{m} - F_\mathrm{m}')/F_\mathrm{m}'$, where F and F_m' are the steady-state and maximum fluorescence intensities in light-acclimated cells (respectively), F_m is the maximal fluorescence intensity in dark-adapted cells, and I is the light irradiance in μmol quanta m^{-2} s^{-1} (refs 36, 37). In Fig. 2c and Extended Data Fig. 4a, d, the light irradiance is 30 μmol quanta m^{-2} s^{-1}. The light saturation curves of ETR$_\mathrm{PS\,II}$ were fitted with the exponential rise function

$P = P_{max}(1 - \exp(E/E_k))$, where P_{max} is the maximal photosynthetic electron transport rate and E_k is the optimal light. ΔETR/ETR (Fig. 3a) was calculated as $(ETR_{ref} - ETR) \times 100/ETR_{ref}$, the reference being the value measured in wild-type cells in untreated conditions.

Membrane-inlet mass spectrometry measurements. Samples were introduced in a 3 ml thermostated cuvette, which was connected to a Quadrupole Mass Spectrometer (QMS 200, Pfeiffer Vacuum Prisma) by a stainless steel vacuum tube (0.125 inches) passing through a water trap filled with ethanol and dry ice. The sample was separated from the tube via a gas-permeable inlet system (polytetrafluoroethylene (PTFE) membrane). $^{18}O_2$ was added as a bubble to the algal suspension, and the bubble was removed before the experiment. The measurements of the partial pressures of $^{16}O_2$ ($p^{16}O_2$, $m/z = 32$), $^{18}O_2$ ($p^{18}O_2$, $m/z = 36$) and argon ($m/z = 40$) were performed after the cuvette was sealed. A blue light-emitting diode (LED) source was connected to the cuvette, and the light irradiance was manually adjustable in the 0 to ~800 μmol quanta m^{-2} s^{-1} range. The temperature was kept at $19 \pm 1\,^{\circ}$C in the cuvette during the experiment.

To calculate gross O_2 production (E_0) and uptake (U_0), respectively production and consumption by the cells, we adapted the equations from ref. 38:

$$U_0 = (\Delta[^{18}O]/\Delta t + k[^{18}O])(([^{18}O] + [^{16}O])/[^{18}O])$$

$$E_0 = (\Delta[^{16}O]/\Delta t + k[^{16}O]) + U_0(([^{18}O] + [^{16}O])/[^{16}O])$$

where k is the rate constant of O_2 decrease measured in the absence of algae. We normalized O_2 to Argon (a biologically inert gas with very similar solubility properties), which decreases the sensitivity of O_2 measurements to fluctuations by ~80% (ref. 39). The gas concentrations were calibrated by measuring the air-equilibrated O_2 concentration (stirring deionized water in the open cuvette for at least 5 h) and background O_2 (bubbling with N_2).

Respiration rates. Respiration rates were measured as O_2 exchange rates using a Clark-type oxygen electrode at 19 $^{\circ}$C (Hansatech Instruments). AOX capacity was measured as SHAM-sensitive respiration in conditions where the cyanide-sensitive pathway was inhibited beforehand (AA, 5 μM).

ATP/NADPH *in vivo* measurements. NADP$^+$/NADPH redox changes were followed in living cells using a Dual-PAM (Walz). NADPH fluorescence was measured at 460 nm, upon excitation in the near ultraviolet. Chlorophyll *a* concentration was ~5 μg ml^{-1}. ATP content was measured using an *in vivo* ^{31}P-AMX 400 NMR spectrometer equipped with a 25-mm multinuclear probe tuned at 161.9 MHz, and a homemade lighting system, as described in ref. 40. The relative ATP content was estimated *in vivo* from the surface of α-, β- and γ-phosphorus resonance peaks corresponding to the three phosphates of NTPs, which dominate the NMR spectra with inorganic phosphate and polyphosphates[41].

Western blots and immunolocalization. Protein samples (5–10 μg) were loaded on 13% SDS–polyacrylamide gel electrophoresis (PAGE) gels and blotted to nitrocellulose. Primary AOX antibody was custom designed (Sdix, 1:4,000 dilution). All other antisera used were obtained from Agrisera (http://www.agrisera.com/en/info/catalog.html). The blots were developed with ECL detection reagent and images of the blots were obtained using a CCD (charge-coupled device) imager (Chemidock MP Imaging, Bio-Rad). The results presented in Fig. 3b are representative of a total of five western blots on independent biological samples. Immunolocalization of AOX was generally done as described in ref. 34. Briefly, cells were fixed with 2% formaldehyde in culture media for 20 min, washed three times with marine phosphate buffer (mPBS, see ref. 42) and permeabilized by 1% Triton X-100 in mPBS for 10 min. The cells were washed again, blocked for 30 min in 1% BSA in mPBS, and incubated overnight at room temperature (25 $^{\circ}$C) with anti-AOX antibody from rabbit (custom design, Sdix, 1:200 dilution in mPBS). The cells were then rinsed with mPBS and incubated with donkey Alexa 488-conjugated anti-rabbit IgG antibody (Life Technologies, at 1:100 dilution in mPBS) for 2 h at room temperature. Cells were then stained with 0.5 μg ml^{-1} DAPI (4′,6′-diamidino-2-phenylindole, Life Technologies) for 10 min and mounted with Vectashield (Vector Laboratories) after a rinse. Finally the cells were observed using a Leica SP5 confocal microscope (Leica Microsystems).

Electron microscopy. For transmission electron microscopy, *P. tricornutum* cells were fixed in 0.1 M cacodylate buffer (Sigma-Aldrich), pH 7.4, containing 2.5% glutaraldehyde (TAAB), 2% formaldehyde (Polysciences) for 1 h at room temperature and then prepared according to a modified protocol from T. J. Deerinck *et al.* (http://ncmir.ucsd.edu/sbfsem-protocol.pdf). After the dehydration steps, the cells were infiltrated with ethanol/Epon resin mixture (2/3–1/3

for 1 h and 1/3–2/3 for 1 h) and finally embedded in Epon in a 60 $^{\circ}$C oven for 48 h or longer. Ultrathin sections (60 nm) were prepared with a diamond knife on an UC6 Leica ultramicrotome and collected on 200 μM mesh nickel grids before examining on a JEOL 1200 EX electron microscope.

AOX knockdown lines. Partial coding sequence of AOX (identity Phatr2_bd1075) was amplified using primers AOXcFwd (TGCTCCGGAGGACAAT GAATTCGC) and AOXcRev (TGGTCTAGACGTCGCGATGTTC), cut by EcoRI/XbaI (Fermentas) and cloned into an EcoRI/XbaI-digested antisense construct[43], under control of the FcpB promoter. The AOX antisense construct was introduced into wild-type *P. tricornutum* cells using the standard microparticle bombardment procedure with a PDS-1000/He Particle Delivery System (Bio-Rad)[43,44]. After 2 days, cells were transferred to F/2-supplemented–filtered seawater plates containing 100 μg ml^{-1} phleomycin, a selective antibiotic for the *Sh ble* gene (InvivoGen, 09K30-MM). Putative antisense lines were verified for the presence of the transformed DNA by PCR screening using the primers ShbleFwd (ACCAGTGCCGTTCCGGTG) and ShbleRev (TCGGTCAGTCCTGCTCCTC), and the most strongly silenced lines were chosen on the basis of reduction of AOX protein levels as measured by SDS–PAGE western blot with an anti-AOX antibody (see section on western blots and immunolocalization).

25. Vartanian, M., Desclés, J., Quinet, M., Douady, S. & Lopez, P. J. Plasticity and robustness of pattern formation in the model diatom *Phaeodactylum tricornutum*. *New Phytol.* **182,** 429–442 (2009).
26. Guillard, R. R. L. in *Culture of Marine Invertebrate Animals* (eds Smith W. L. & Chanley M. H.) 26–60 (Plenum, 1975).
27. Joët, T., Cournac, L., Horvath, E. M., Medgyesy, P. & Peltier, G. Increased sensitivity of photosynthesis to antimycin A induced by inactivation of the chloroplast *ndhB* gene. Evidence for a participation of the NADH-dehydrogenase complex to cyclic electron flow around photosystem I. *Plant Physiol.* **125,** 1919–1929 (2001).
28. Wishnick, M. & Lane, M. D. Inhibition of ribulose diphosphate carboxylase by cyanide. Inactive ternary complex of enzyme, ribulose diphosphate, and cyanide. *J. Biol. Chem.* **244,** 55–59 (1969).
29. Nakano, Y. & Asada, K. Purification of ascorbate peroxidase in spinach chloroplasts; its inactivation in ascorbate-depleted medium and reactivation by monodehydroascorbate radical. *Plant Cell Physiol.* **28,** 131–140 (1987).
30. Asada, K., Takahashi, M. A. & Nagate, M. Assay and inhibitors of spinach superoxide dismutase. *Agric. Biol. Chem.* **38,** 471–473 (1974).
31. Joliot, P. & Delosme, R. Flash induced 529 nm absorption change in green algae. *Biochim. Biophys. Acta* **357,** 267–284 (1974).
32. Santabarbara, S., Redding, K. E. & Rappaport, F. Temperature dependence of the reduction of p-700$^+$ by tightly bound plastocyanin *in vivo*. *Biochemistry* **48,** 10457–10466 (2009).
33. Melis, A. Kinetic analysis of P-700 photoconversion: effect of secondary electron donation and plastocyanin inhibition. *Arch. Biochem. Biophys.* **217,** 536–545 (1982).
34. Bailleul, B., Cardol, P., Breyton, C. & Finazzi, G. Electrochromism: a useful probe to study algal photosynthesis. *Photosynth. Res.* **106,** 179–189 (2010).
35. Johnson, X. *et al.* A new setup for *in vivo* fluorescence imaging of photosynthetic activity. *Photosynth. Res.* **102,** 85–93 (2009).
36. Genty, B., Briantais, J. M. & Baker, N. R. The relationship between the quantum yield of photosynthetic electron transport and quenching of chlorophyll fluorescence. *Biochim. Biophys. Acta* **990,** 87–92 (1989).
37. Bilger, W. & Björkman, O. Role of the xanthophyll cycle in photoprotection elucidated by measurements of light-induced absorbance changes, fluorescence and photosynthesis in leaves of *Hedera canariensis*. *Photosynth. Res.* **25,** 173–186 (1990).
38. Peltier, G. & Thibault, P. O$_2$ uptake in the light in *Chlamydomonas*. *Plant Physiol.* **79,** 225–230 (1985).
39. Kana, T. M. *et al.* A membrane inlet mass spectrometer for rapid and high-precision determination of N$_2$, O$_2$, and Ar in environmental water samples. *Anal. Chem.* **66,** 4166–4170 (1994).
40. Rivasseau, C. *et al.* Accumulation of 2-*C*-methyl-D-erythritol 2,4-cyclodiphosphate in illuminated plant leaves at supraoptimal temperatures reveals a bottleneck of the prokaryotic methylerythritol 4-phosphate pathway of isoprenoid biosynthesis. *Plant Cell Environ.* **32,** 82–92 (2009).
41. Bligny, R. & Douce, R. NMR and plant metabolism. *Curr. Opin. Plant Biol.* **4,** 191–196 (2001).
42. Van de Meene, A. M. L. & Pickett-Heaps, J. D. Valve morphogenesis in the centric diatom *Rhizosolenia setigera* (Bacillariophyceae, Centrales) and its taxonomic implications. *Eur. J. Phycol.* **39,** 93–104 (2004).
43. De Riso, V. *et al.* Gene silencing in the marine diatom *Phaeodactylum tricornutum*. *Nucleic Acids Res.* **37,** e96 (2009).
44. Falciatore, A., Casotti, R., Leblanc, C., Abrescia, C. & Bowler, C. Transformation of nonselectable reporter genes in marine diatoms. *Mar. Biotechnol. (NY)* **1,** 239–251 (1999).

a

b
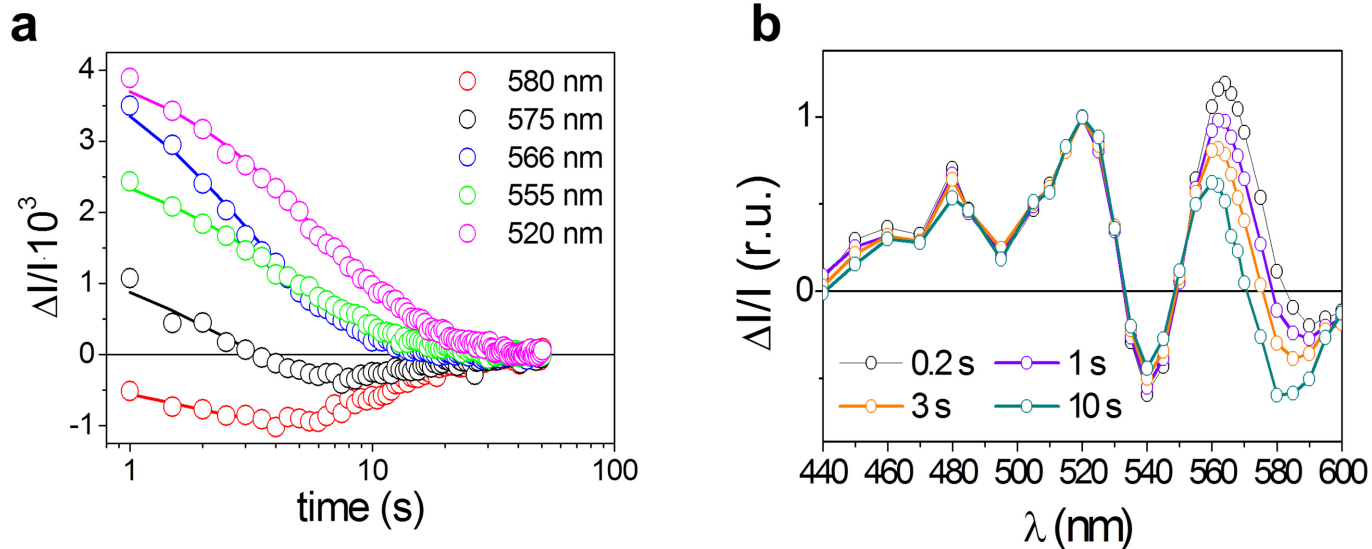
Extended Data Figure 1 | Deconvolution of the quadratic and linear ECS in *P. tricornutum*. a, Absorption difference ($\Delta I/I$) kinetics followed at different wavelengths in *P. tricornutum*, after a series of six saturating laser flashes, in anaerobic conditions. Solid lines correspond to the global fit of the experimental data with a sum of two exponential decays, with time constants τ and 2τ, respectively, as expected for linear and quadratic dependencies (see Methods). **b**, $\Delta I/I$ spectra are shown at different times during ECS relaxation. All spectra were normalized to 1 at 520 nm for better comparison. The observation that the blue and green parts of the spectrum are homothetic during relaxation, while changes are seen in the red most part of it, reflects the presence of the two ECS components, having different relaxation kinetics.
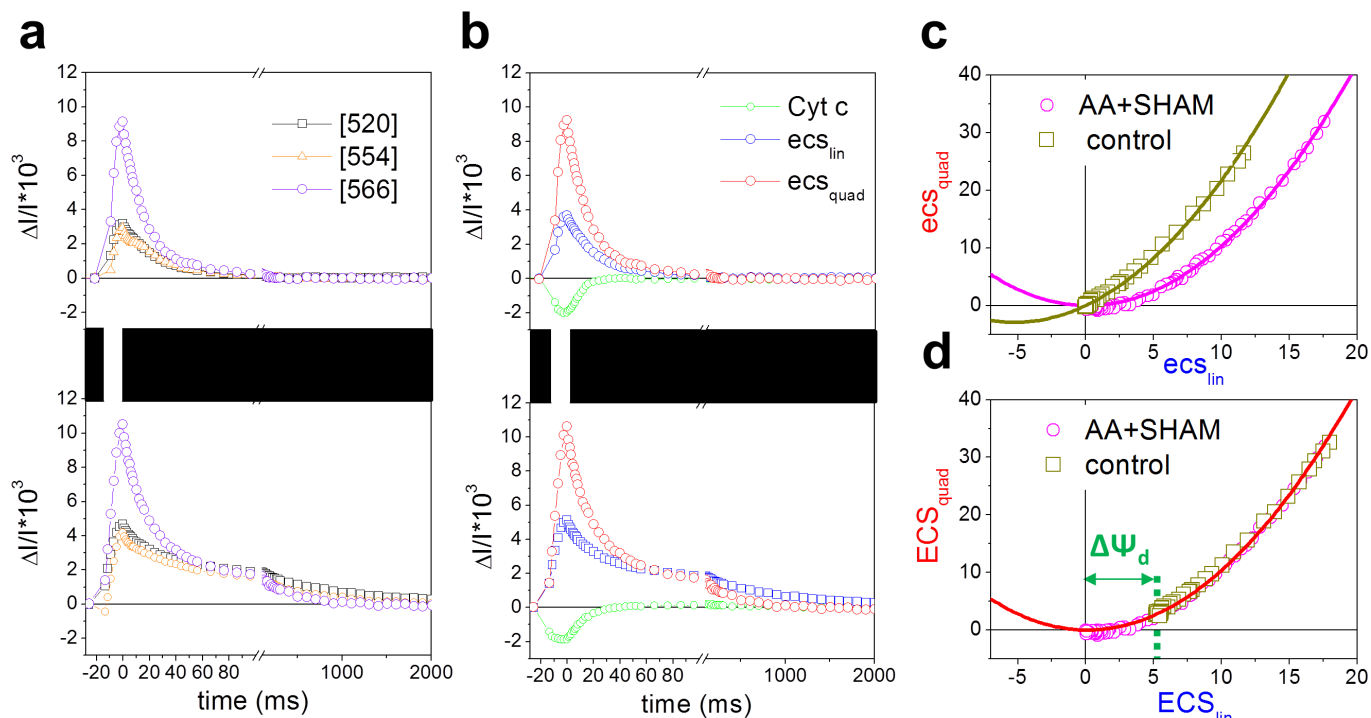
Extended Data Figure 2 | Separation of *c*-type cytochrome signals from linear and quadratic ECS signals in *P. tricornutum*. a, Kinetics of $\Delta I/I$ changes at 520, 554 and 566 nm during an ~10 ms pulse of saturating red light (4,500 µmol quanta $m^{-2} s^{-1}$) and the subsequent dark relaxation (top: control conditions; bottom: AA + SHAM). **b**, Kinetics of ecs_{lin}, ecs_{quad} changes and *c*-type cytochrome redox state, from kinetics in **a**, after deconvolution as explained in Methods. **c**, **d**, Relationship between the quadratic and the linear ECS, before (ecs_{lin}, ecs_{quad}, **c**) and after (ECS_{lin}, ECS_{quad}, **d**) correction for the dark electric field (see Methods). Dark yellow and magenta symbols correspond to control and AA + SHAM conditions, respectively. The green arrow indicates the value of $\Delta \Psi_d$ in control conditions. Data are representative of five independent biological samples. The black boxes in **a** and **b** indicate periods of darkness.
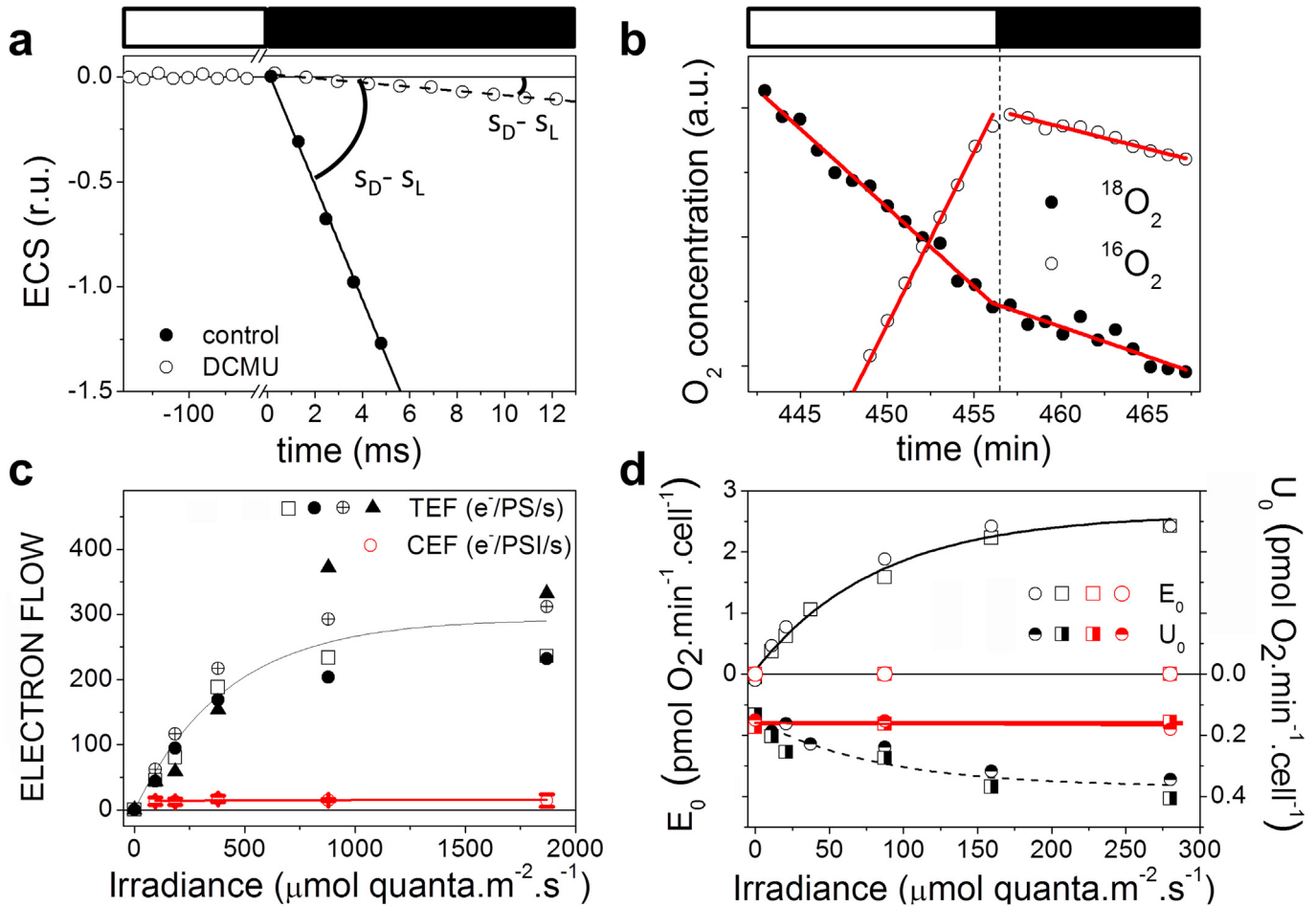
Extended Data Figure 3 | Cyclic electron flow and water-to-water cycles in *P. tricornutum*. a, Representative traces of changes in ECS_{lin} (normalized as explained in Methods, namely expressed in charge separation per PS) to evaluate linear and cyclic electron flow. Cells were illuminated with 1,870 μmol quanta m^{-2} s^{-1} of red light, in absence (filled circles) and presence (open circles) of DCMU and then transferred to the dark; r.u., relative units. **b**, Representative traces of the $^{16}O_2$ and $^{18}O_2$ concentrations at the offset of a 280 μmol quanta m^{-2} s^{-1} blue light; a.u., arbitrary units. In **a** and **b**, light and dark periods are represented by white and black boxes, respectively. **c**, Photochemical rate corresponding to total electron flow (TEF, dark symbols, data from four independent biological samples) and CEF (red symbols, $n = 8 \pm$ s.d.) at different irradiances. TEF and CEF were estimated from the initial slope of the ECS decay, as ($S_D - S_L$ control) and ($S_D - S_L$ DCMU), respectively (see Methods). **d**, Light-dependencies of oxygen uptake (U_0, half-filled symbols) and gross photosynthesis (E_0, open symbols) in control conditions (dark) and in the presence of DCMU (red). Data from two independent biological samples (squares and circles).
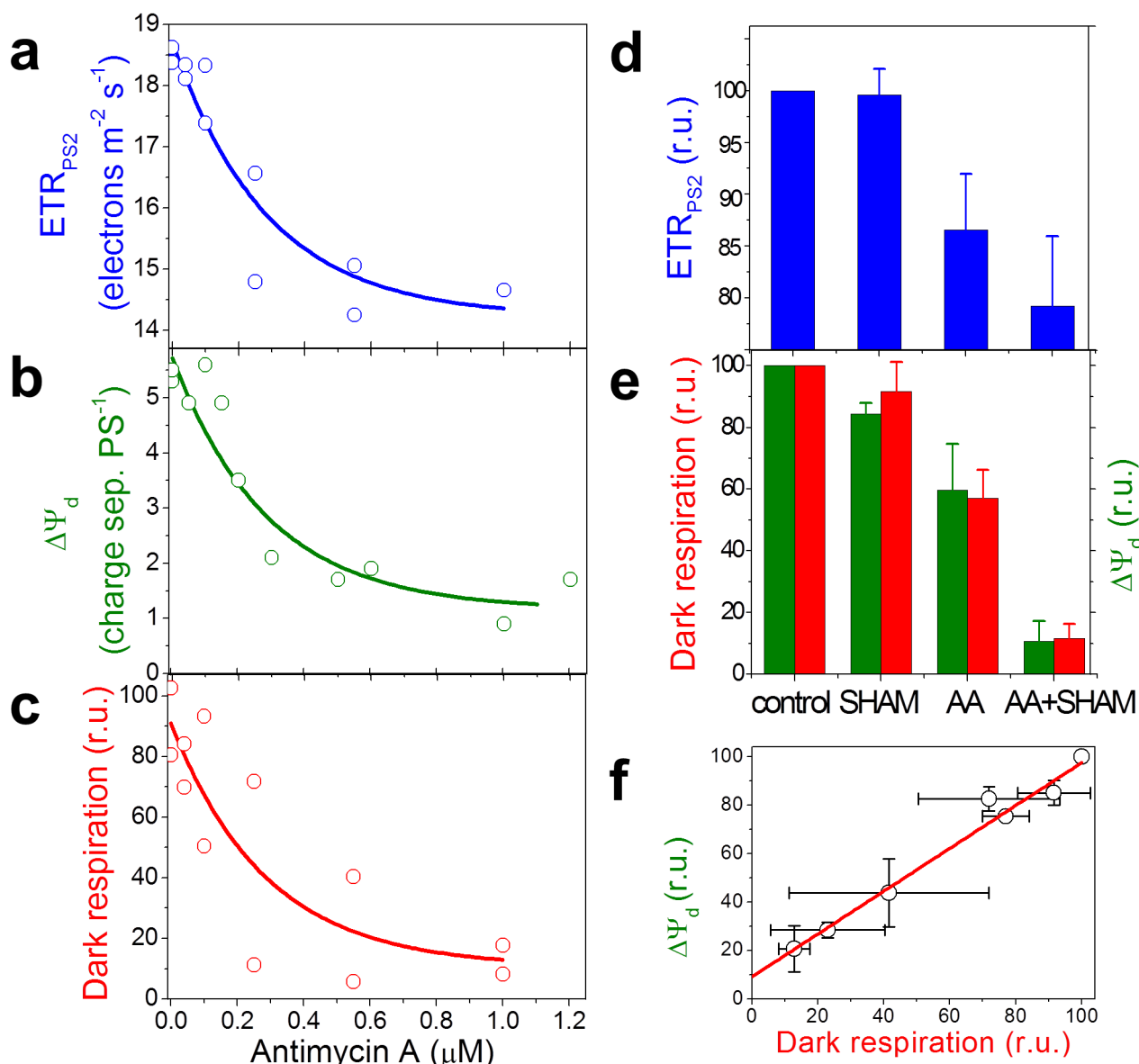
Extended Data Figure 4 | $\Delta\Psi_d$ and photosynthesis under respiratory inhibition in *P. tricornutum*. **a–c**, Dependency of the $ETR_{PS\,II}$ (**a**), $\Delta\Psi_d$ (**b**) and dark respiration (**c**) upon inhibition of the cyanide-sensitive respiratory pathway with different concentrations of antimycin A, in the presence of saturating SHAM (1 mM). Data from two independent biological samples. Experimental data were fitted with a mono-exponential decay function.

d, e, $ETR_{PS\,II}$ (**d**), $\Delta\Psi_d$ and dark respiration (**e**), expressed as percentage of control, in the presence of saturating AA (5 µM), SHAM (1 mM) or AA + SHAM (four independent experiments ± s.d.). **f**, Relationship between $\Delta\Psi_d$ and mitochondrial respiration in samples treated with increasing concentrations of AA in the presence of 1 mM SHAM (mean value ± s.e.m. from **b** and **c**).
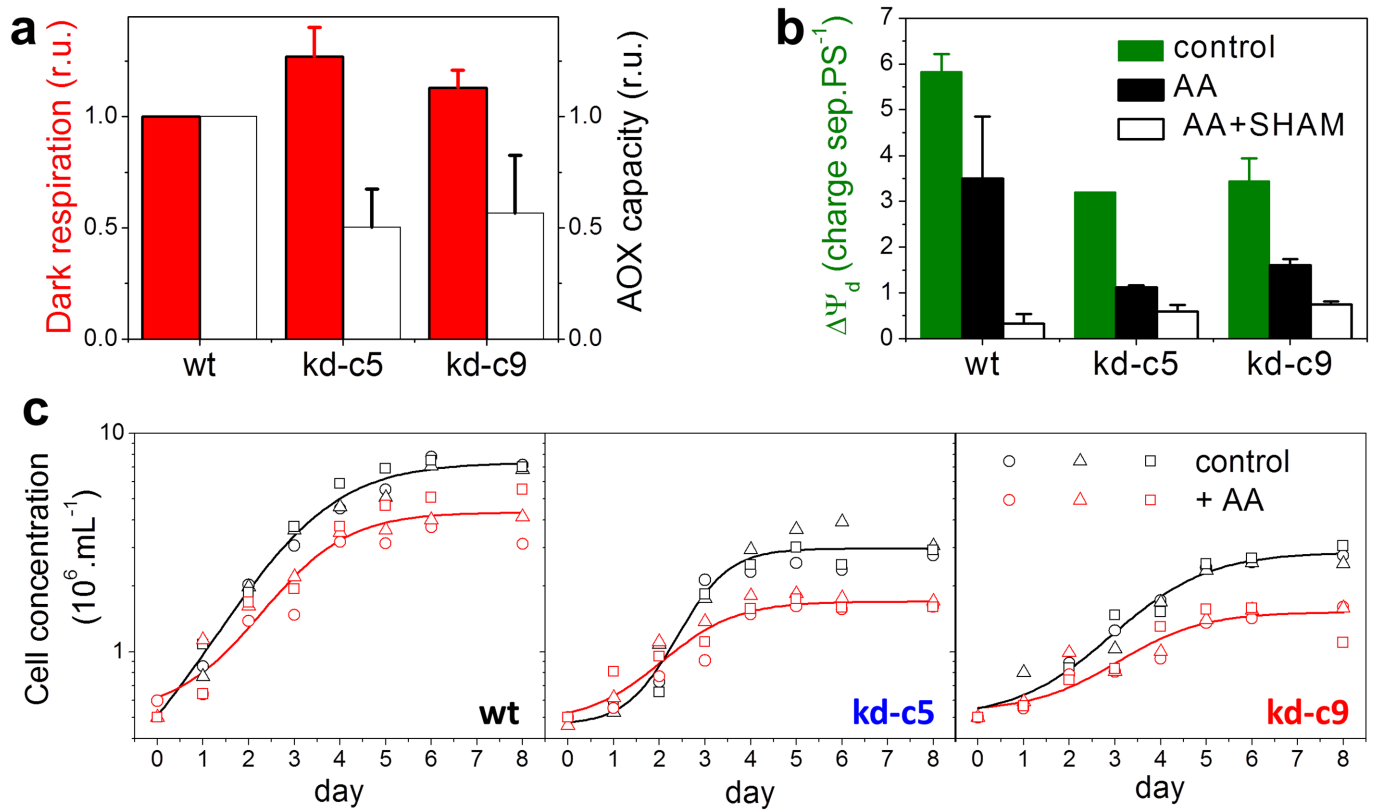
Extended Data Figure 5 | Dark respiration, PMF and growth in AOX knockdown lines of *P. tricornutum*. **a**, Respiratory activity of wild-type and AOX knockdown lines. Total respiration rate (red bars) and the contribution of the AOX capacity (white bars, see Methods) were normalized to wild-type values ($n = 5 \pm$ s.d.). **b**, ECS-based measurements of $\Delta\Psi_d$ in wild-type ($n = 3 \pm$ s.d.) and AOX knockdown lines ($n = 2 \pm$ s.e.m.), in control conditions (green), in the presence of AA (dark green) and in the presence of AA + SHAM (white). **c**, Growth curves of wild-type and AOX knockdown lines in the presence/absence of AA ($2\,\mu$M). Three independent growth curves are shown for each strain/condition. AA was added every day and cells were grown in continuous light to prevent them from dying in the dark because of lack of respiration.

a

Green: Alexa (AOX)
Red: Chlorophyll (chloroplast)

Blue: DAPI (nucleus)

b
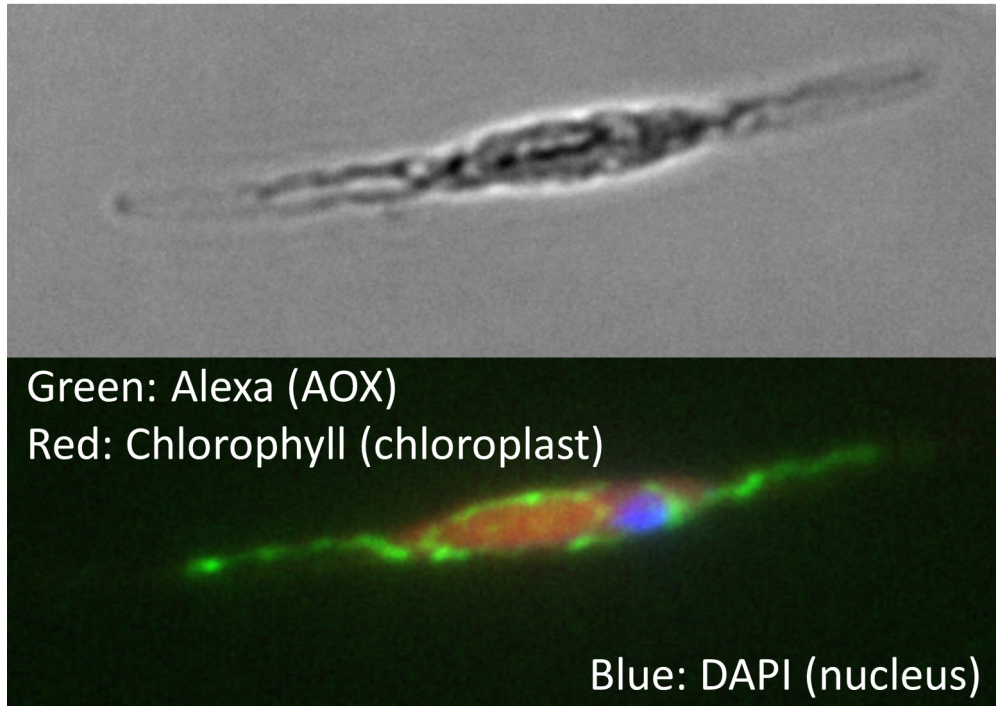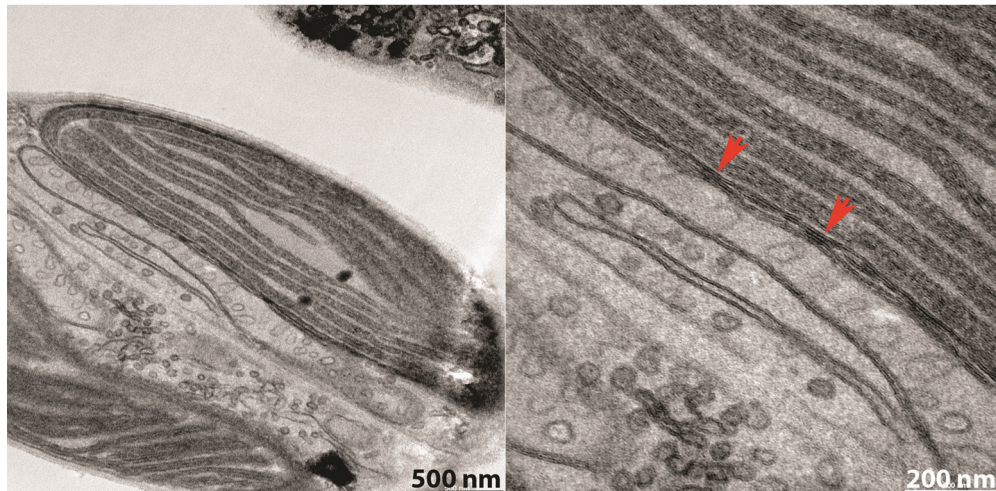
**Extended Data Figure 6 | Subcellular localization of AOX in *P. tricornutum* and plastid–mitochondria interaction in *P. tricornutum* wild-type cells.** **a**, Subcellular localization of AOX. Cells were treated with an anti-AOX antibody and then with a secondary Alexa Fluor 488 antibody (see Methods). Positions of plastid and nuclei are indicated by chlorophyll *a* autofluorescence (red) and DAPI staining (blue), respectively. The pattern of AOX localization is highly similar to that observed with the mitochondria-specific mito-tracker probe (data not shown). Images are representative of 60 cells from three independent biological samples. **b**, Electron micrographs of the plastid–mitochondria juxtaposition in *P. tricornutum*. Arrows indicate possible physical contacts between the plastid and mitochondrial membranes. Image is representative of 51 images from seven independent biological samples.
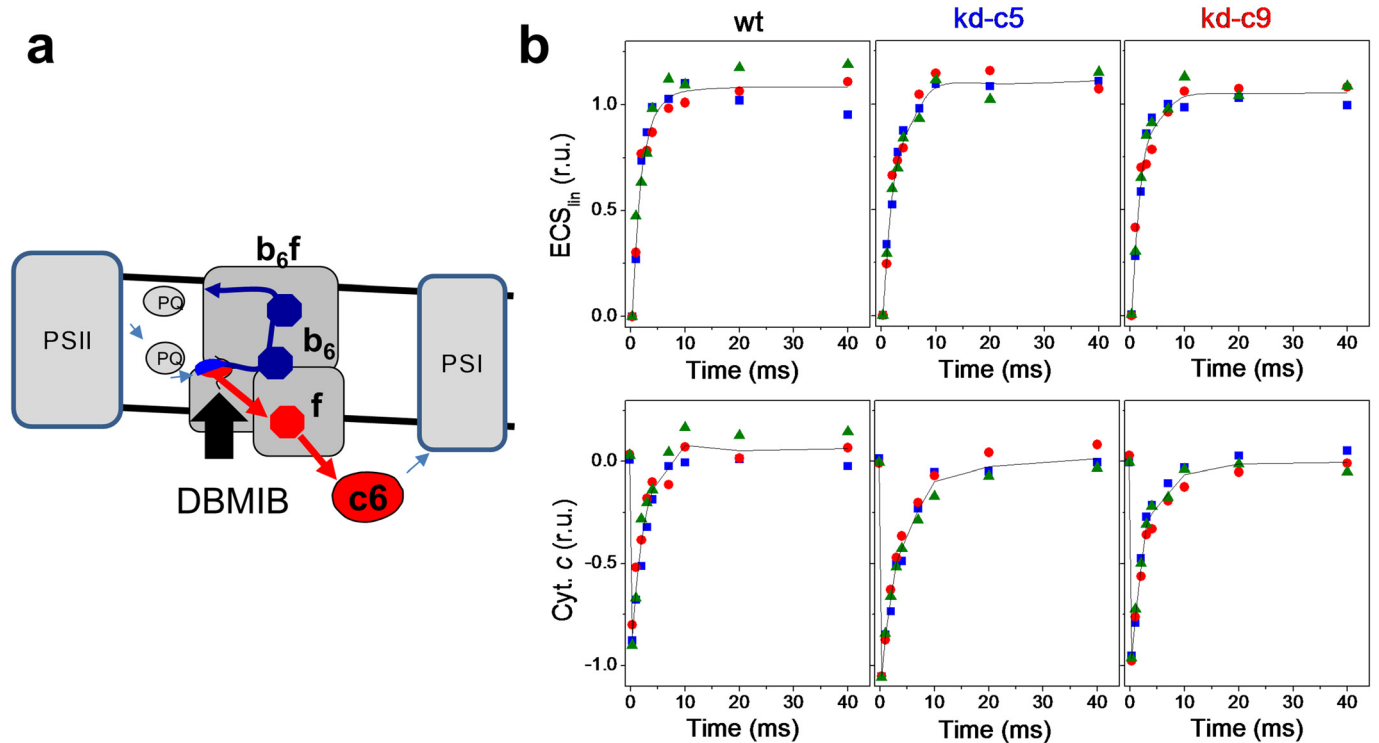
Extended Data Figure 7 | Cytochrome b_6f turnover in *P. tricornutum* wild-type and AOX knockdown lines. a, Schematic representation of the electron-flow reaction steps in the cytochrome b_6f complex, which can be evaluated by spectroscopic measurements. **b**, Slow phase of ECS_{lin} indicating cytochrome b_6 activity (top) and time-resolved redox changes of cytochromes c_6/f (bottom) in wild-type and AOX knockdown lines (kd-c5 and kd-c9). *P. tricornutum* cells were exposed to saturating single-turnover laser flashes given 10 s apart. Data were normalized to the amplitude of the fast phase of the ECS_{lin} signal. Cytochrome c and ECS_{lin} were deconvoluted as explained in Methods. Three independent biological samples are shown in red, blue and green colours. Cell concentration was 2×10^7 cells per millilitre. Note that both the slow phase of the ECS_{lin} and the reduction of cytochromes c_6/f were completely abolished by the plastoquinone competitive inhibitor DBMIB (10 µM; black arrow).
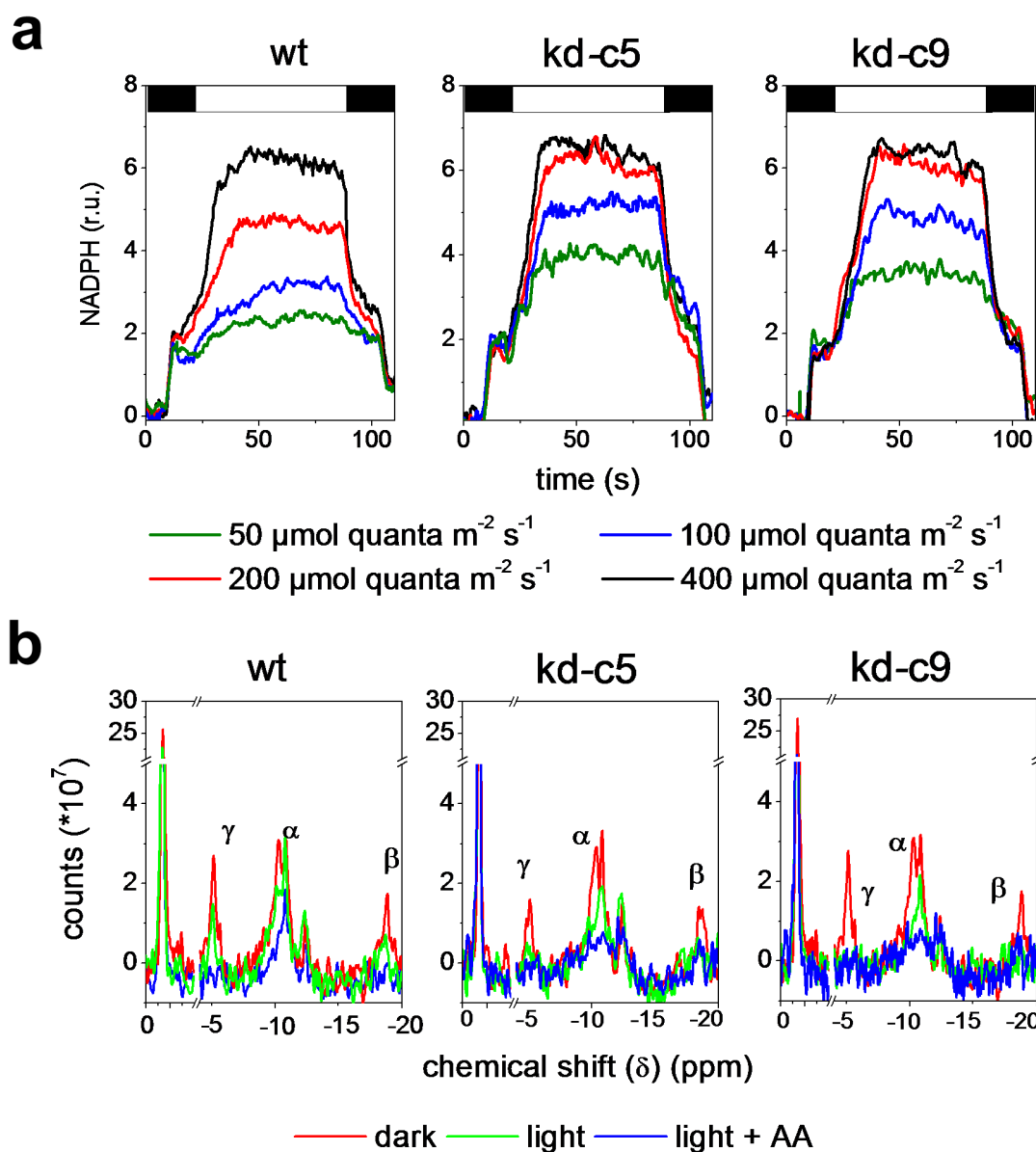
Extended Data Figure 8 | *In vivo* changes in the NADPH redox state and ATP in wild-type and AOX knockdown lines. a, Changes in NADPH at different light intensities. Light and dark periods are represented by white and black boxes, respectively. Light intensities were 50, 100, 200 and 400 μmol quanta m^{-2} s^{-1} (green, blue, red, and black traces, respectively). Chlorophyll concentration was ~5 μg ml^{-1}. **b**, Spectra from cells of wild-type (left) and AOX knockdown lines c5 (middle) and c9 (right) in the dark (red), light (green) and light + AA (blue) conditions are shown, with normalization to the internal standard (methylenediphosphonate; pH 8.9). The positions of the α-, β- and γ-phosphates of NTPs are shown. **a**, **b**, Representative of three independent biological samples.
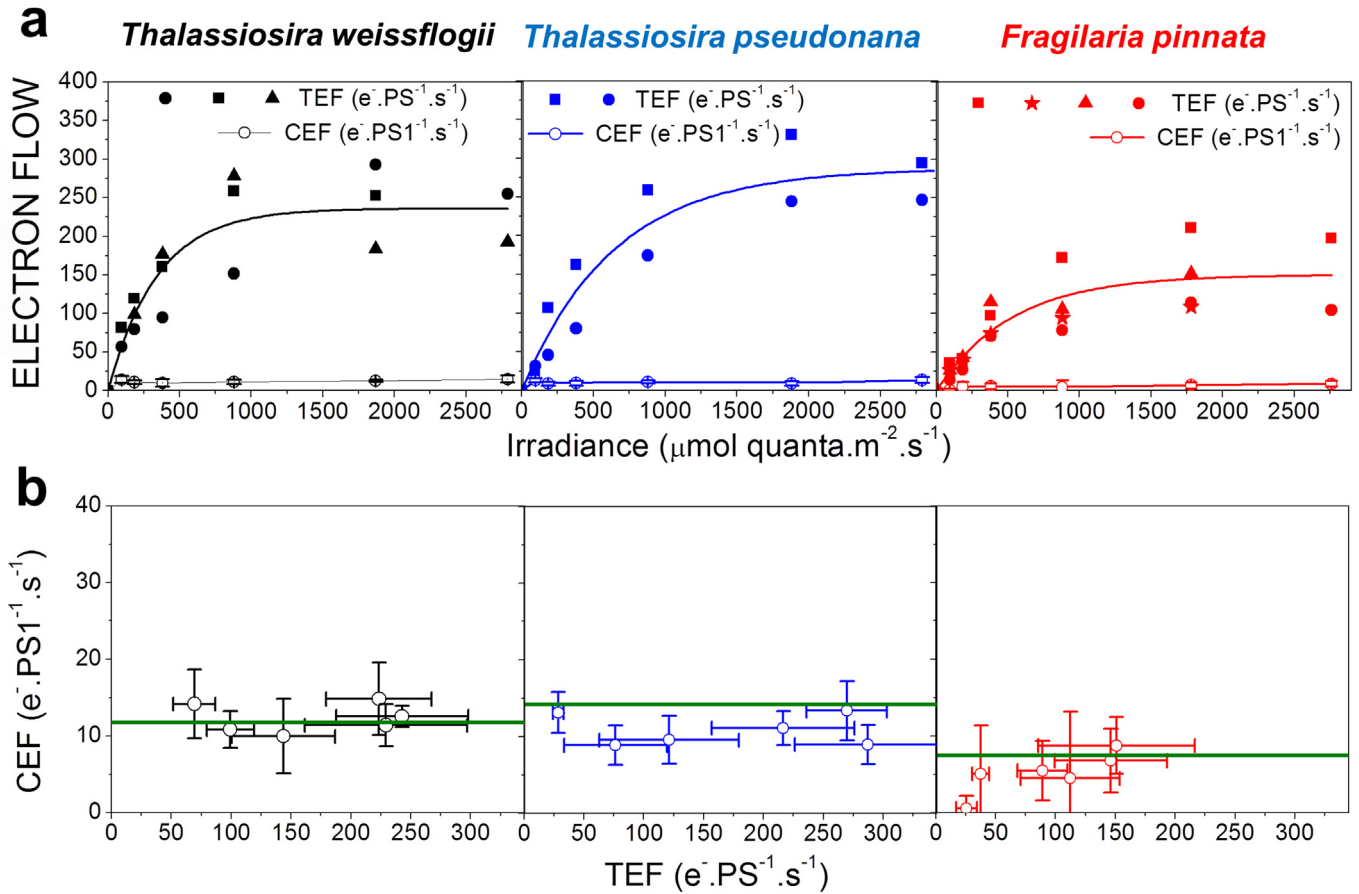
Extended Data Figure 9 | Cyclic electron flow in representative diatoms.
a, Total electron flow (filled symbols) was measured at different light irradiances, as illustrated in Extended Data Fig. 3, in *T. weissflogii* (black, *n* = 3 independent biological samples), *T. pseudonana* (blue, *n* = 2) and *F. pinnata* (red, *n* = 4). Cyclic electron flow capacity was also measured for every species (open circles, five independent biological samples ± s.d.). **b**, CEF capacity was plotted against TEF. CEF and TEF are presented as mean values ± s.d. from **a**. The green line corresponds to CEF = 5% of the maximal total electron flow.
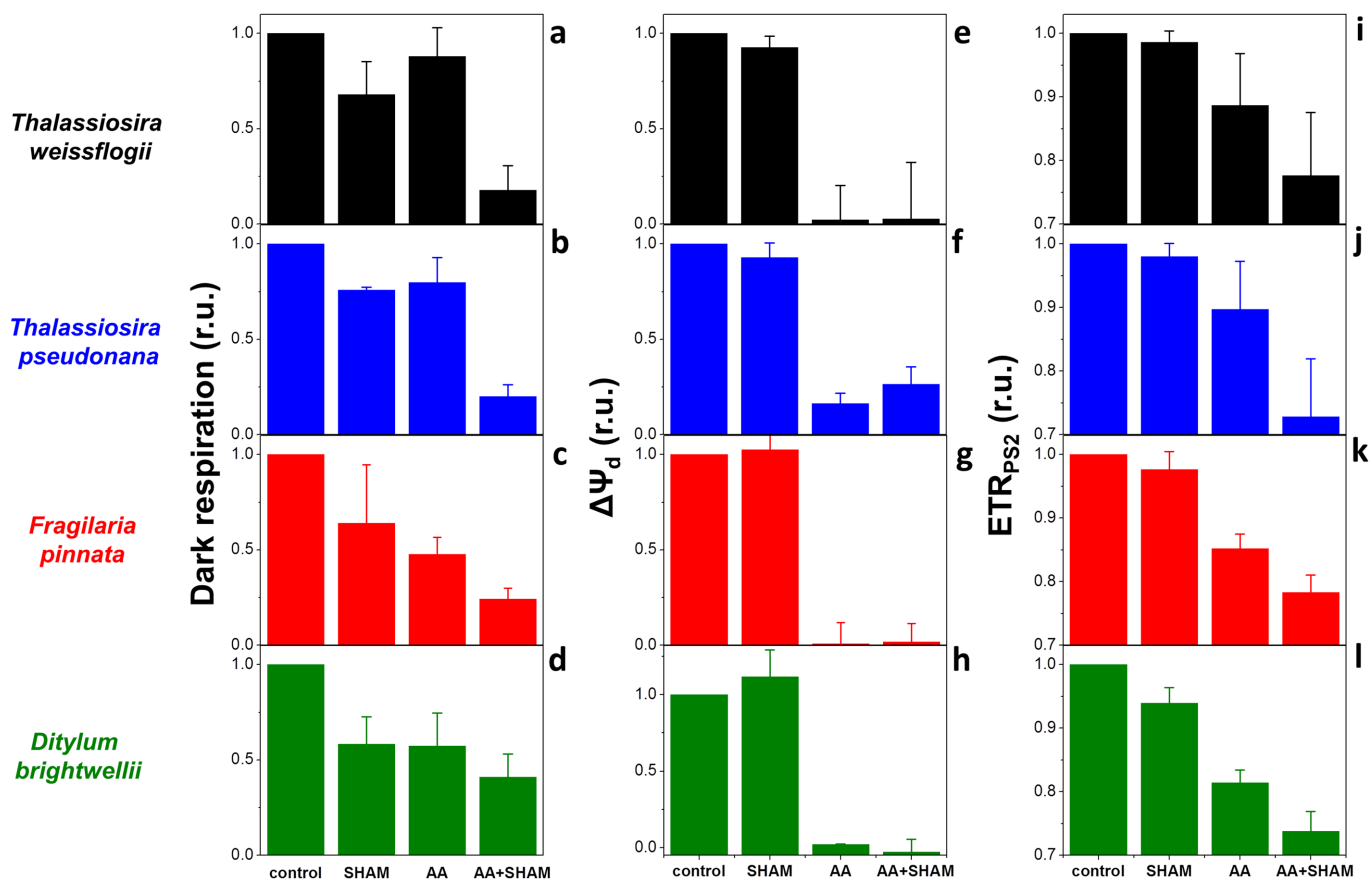
Extended Data Figure 10 | $\Delta \varPsi_d$ and photosynthesis under conditions of respiratory inhibition in representative diatoms. Dark respiration (**a**–**d**), $\Delta \varPsi_d$ (**e**–**h**) and $ETR_{PS\ II}$ (**i**–**l**) in untreated cells and after treatment with inhibitors of respiration antimycin A, and/or SHAM at saturating concentrations. **a**, **e**, **i**, *T. weissflogii* (black). **b**, **f**, **j**, *T. pseudonana* (blue). **c**, **g**, **k**, *F. pinnata* (red). **d**, **h**, **l**, *D. brightwellii* (green). The data represent the mean value ± s.d. of three (**l**), four (**d**), five (**f**, **h**, **k**), six (**a**, **c**, **e**, **j**), seven (**b**, **i**) or eight (**g**) independent experiments. All data were normalized to the control value.